ROYAL SOCIETY OF CHEMISTRY

Check for updates

A new azo dye for colorimetric determination of lead(II) ions†

Sefiu Olalekan Olaleye [ID] *[ab] and Uzma Bibi [ID] [c]

A new azo dye, **S9b** (1-amino-4-[(E)-2-(8-hydroxyquinolin-5-yl)diazen-1-yl]-9,10-dihydroanthracene-9,10-dione), was developed and evaluated as a colorimetric chemosensor for lead(II) ions. Upon Pb^{2+} addition, the **S9b** solution color changed from rosy-brown to sandy-brown. The UV-vis spectrum of the **S9b**–Pb^{2+} complex exhibited a hyperchromic shift compared to free **S9b** and a bathochromic shift relative to **S9b** complexes with other metal ions. Optimized conditions comprised an ethanol solvent system, pH 6.0, a reaction time of 2 min, and a 2 : 1 molar ratio of **S9b** to Pb^{2+}. The response of **S9b** was linear at Pb^{2+} concentrations of 3.90–9.36 µg mL^{-1}. The calculated detection limit, quantitation limit and binding constant were 1.55 µg mL^{-1}, 4.71 µg mL^{-1} and 3.07×10^4 L^2 g^{-2}, respectively. Determination of Pb^{2+} was not significantly affected by other interfering cations (Ag^+, Co^{2+}, Cu^{2+}, Fe^{2+}, Fe^{3+}, Na^+, K^+, Ni^{2+}, Hg^{2+}, Ca^{2+}, Zn^{2+}, Mg^{2+}, and Al^{3+}). The **S9b**-based method demonstrated recoveries of 100.03–103.11% and relative standard deviations (RSDs) of 0.06–2.07% for Pb^{2+} in spiked water samples, with accuracy and precision comparable to atomic absorption spectroscopy (AAS). FTIR studies and DFT calculations indicated that Pb^{2+} binding to **S9b** occurs *via* the heterocyclic nitrogen and phenolic hydroxyl groups of the azo dye. The sensor demonstrated reusability following regeneration with EDTA, which dissociated the Pb^{2+} complex. This study highlights the potential of the anthracene-9,10-dione-based azo dye as a simple, eco-friendly, and rapid chemosensor for Pb^{2+} detection in aqueous systems.

1. Introduction

Water contamination by heavy metals poses significant risks to human health and ecosystems. Among these metals, lead (Pb) is particularly hazardous, exerting toxic effects even at trace concentrations. Lead(II) ions are extensively utilized in industries such as battery manufacturing, automotive production, paints, ceramics, and mining.[1–4] Environmental Pb^{2+} contamination primarily occurs through rainwater-mediated leaching of soil particles contaminated by anthropogenic activities. The World Health Organization (WHO) stipulates a guideline value of 10 µg L^{-1} for lead in drinking water, underscoring its acute toxicity.[5] Chronic exposure to Pb^{2+} induces severe renal and neurological damage,[4] disrupts reproductive systems in both sexes (reducing sperm count, motility, and altering morphology),[6,7] and is linked to adverse pregnancy outcomes, including miscarriage, preterm birth, and developmental deficits.[8] At the cellular level, Pb^{2+} interferes with DNA transcription and compromises membrane integrity,[9] necessitating robust environmental monitoring strategies.

Conventional analytical techniques for Pb^{2+} detection, such as atomic absorption/emission spectrometry (AAS/AES), inductively coupled plasma mass spectrometry (ICP-MS), and anodic stripping voltammetry (ASV), offer high sensitivity but are hindered by operational complexity, high cost, and huge technicality.[10–16] Consequently, chemosensors—particularly colorimetric probes—have emerged as promising alternatives due to their simplicity, cost-effectiveness, and potential for real-time field applications.

Azo dyes, widely employed in the textile industry,[17] are gaining attention as colorimetric chemosensors owing to their distinct chromogenic properties. Despite numerous optical sensors reported for Pb^{2+} ion detection,[18–24] a comprehensive literature review highlights that azo-functionalized systems, in particular, remain significantly underexplored for Pb^{2+} detection. For instance, Ghorbanian *et al.*[25] developed a benzothiazole azo dye for Pb^{2+} sensing in DMSO-water (1 : 4 v/v, pH 7), exhibiting a 72 nm hypsochromic shift (blue to pink) with a detection limit of 0.67 µM. Similarly, Wang *et al.*[26] reported an azobenzene-based sensor in acetonitrile-water (1 : 1 v/v, pH 7.21), achieving a limit of detection (LOD) of 5.44 µM *via* a yellow-to-magenta transition. While these systems demonstrate feasibility, dimethylsulfoxide and acetonitrile utilized as sensing milieus are not eco-friendly.

aDepartment of Pharmaceutical Chemistry, Faculty of Pharmacy, University of Ibadan, Orita UI, Ibadan, 200284, Nigeria. E-mail: solaleye5@gmail.com

bDepartment of Pharmaceutical and Medicinal Chemistry, Faculty of Pharmacy, Federal University Oye-Ekiti, Ekiti, Nigeria

cThird World Center for Science and Technology, H. E. J. Research Institute of Chemistry, International Center for Chemical and Biological Sciences, University of Karachi, Karachi, 75270, Pakistan

† Electronic supplementary information (ESI) available. See DOI: https://doi.org/10.1039/d5ra02486b

Anthracene-9,10-dione derivatives, small organic molecules with high molar absorptivity and visible-region absorbance/emission maxima,[27,28] have shown promise as chemosensors for metal ions.[29–32] However, to our knowledge, no azo-functionalized anthracene-9,10-dione derivatives have been reported for Pb^{2+} detection. In continuation of our efforts in sensor design,[33] we herein present a new, fast and simple azo derivative of 1,4-diaminoanthracene-9,10-dione as a selective colorimetric probe for Pb^{2+} in ethanol.

2. Experimental

2.1 Materials and instrument

All the reagents and chemicals were obtained from BDH, Poole, England. Thin-layer chromatography (TLC) was developed on pre-coated silica gel aluminum plates (Kieselgel 60F254, E. Merck, Germany). ^{1}H NMR and ^{13}C NMR spectra were recorded on Bruker BioSpin GmbH Avance NEO 600 MHz, UK. UV-vis spectral data were acquired on the Spectroquant Pharo 300, Merck, Germany. FTIR spectra data were obtained on FT-IR Spectrometer Spectrum Two PerkinElmer, USA. ESI-MS measurements were recorded on AmaZon speed ESI-Ion trap mass spectrometer (Bruker, UK). The pH of the solution was obtained on pH meter (Hanna, US).

2.2 Methodology

2.2.1 Synthesis and characterization of the S9b azo dye.
The azo dye **S9b** was synthesized *via* diazotization-diazocoupling as follows: 1,4-diaminoanthraquinone (100 mg, 0.42 mmol) was dissolved in 20 mL of 1 M HCl under magnetic stirring for 5 min. Sodium nitrite ($NaNO_2$, 30 mg, 4.35 mmol), dissolved in 5 mL deionized water, was added dropwise to the mixture maintained at 5 °C in an ice bath. The reaction was stirred for 30 min, with reaction progress monitored using starch-iodide paper. A solution of 8-hydroxyquinoline (61 mg, 4.21 mmol) in 1.5 mL of 1 M NaOH and 10 mL deionized water was then introduced. After 20 min of stirring, the pH was adjusted to 2 using dilute HCl, and the reaction was allowed to proceed for 2.5 h. The resulting precipitate was isolated by vacuum filtration, neutralized to pH 7 with 0.1 M NaOH, and washed thoroughly with deionized water. The crude product was purified *via* column chromatography (silica gel, gradient elution: hexane/ethyl acetate → ethyl acetate/methanol) to yield the pure azo dye.

The purified compound was analyzed by Attenuated total reflectance Fourier-transform infrared spectroscopy (ATR-FTIR), ^{1}H/^{13}C nuclear magnetic resonance (NMR; acetone-d_6, 600 MHz), and electrospray ionization mass spectrometry (ESI-MS).

2.3 Chemosensor measurement

A stock solution of **S9b** (2.3428 mM) was prepared by mixing 1.5 mL of **S9b** (1 mg mL^{-1}) with 125 µL of buffer solution. 100 µL of **S9b** solution was added to each vial containing five equivalents of solution of nitrate salts of Ag^+, Co^{2+}, Cu^{2+}, Fe^{2+}, Fe^{3+}, Na^+, K^+, Ni^{2+}, Pb^{2+}, Hg^{2+}, Ca^{2+}, Zn^{2+}, Mg^{2+}, and Al^{3+}. The mixture

was swirled for 60 seconds and made up to 5 mL with ethanol. The color changes were observed, and UV-visible scans of the mixture were recorded between 300 and 700 nm on the UV-visible spectrophotometer. Triplicate measurements were performed to ensure reproducibility.

2.4 Optimization studies

2.4.1 Determination of stoichiometric ratio *via* Job's plot method.
To establish the binding stoichiometry between the chemosensor (**S9b**) and Pb^{2+}, a Job's plot analysis was performed.[34] Aliquots of **S9b** (0, 20, 40, 50, 66, 75, 80, 100, 134, 150, 160, 180, and 200 µL) were introduced into separate vials, followed by addition of an equimolar Pb^{2+} solution to achieve a constant total volume of 200 µL for each mixture. The solutions were vortex-mixed for 10 s and subsequently diluted to a final volume of 5 mL with ethanol. Absorbance measurements were recorded at 500 nm in duplicate. The average absorbance values were plotted against the mole fraction of **S9b** to determine the optimal binding ratio.

2.4.2 Reaction chelation time.
To evaluate the binding kinetics between Pb^{2+} and **S9b**, a solution of Pb^{2+} (66 µL) was added to 134 µL of **S9b** stock solution. The reaction mixture was incubated at 30 °C, and timed intervals (0, 2, 5, 10, 15, 20, 25, and 30 min) to assess the progression of chelation. After each interval, the mixture was diluted to a final volume of 5 mL with ethanol, and absorbance was measured at the maximum absorption wavelength ($\lambda_{max} = 500$ nm). All measurements were performed in triplicate. The average absorbance values were plotted as a function of reaction time to determine the equilibrium time for Pb^{2+}–**S9b** complexation.

2.4.3 Optimization of solvent medium for chemosensing.
To identify the optimal solvent medium for Pb^{2+} detection, **S9b** solution (134 µL) was mixed with 66 µL of Pb^{2+} solution, vortexed for 10 s and incubated for 2 min. The mixture was diluted to a final volume of 5 mL with ethanol, and the resultant colorimetric response was visually assessed. This protocol was replicated using methanol, acetone, dimethyl sulfoxide (DMSO), and N, N-dimethylformamide (DMF) as alternative dilution solvents. Observations of color transitions were recorded to evaluate the best solvent for the Pb^{2+}–**S9b** interaction.

2.4.4 pH optimization for Pb^{2+} detection.
To determine the optimal pH for Pb^{2+} detection, 1.5 mL of **S9b** solution was aliquoted into five separate vials. Each vial was adjusted to a distinct pH (4, 6, 7, 8, or 10) by adding 125 µL of 0.1 M phosphate buffer. Subsequently, 134 µL of the pH-adjusted **S9b** solution was combined with 66 µL of Pb^{2+} solution, vortex-mixed for 10 s, incubated for 2 min and diluted to a final volume of 5 mL with ethanol. Absorbance measurements were recorded at $\lambda_{max} = 500$ nm using a UV-vis spectrophotometer. All experiments were performed in duplicate, and mean absorbance values were plotted against pH to identify the optimal reaction conditions.

2.5 Analytical method development

2.5.1 Linear dynamic range, sensitivity, and detection limits.
To evaluate the linear dynamic range and sensitivity of

the chemosensor, aliquots of Pb^{2+} stock solution (0, 25, 30, 35, 45, 50, 55, and 60 µL) were transferred to eight separate vials. Each aliquot was mixed with 134 µL of **S9b** solution, vortexed for 10 s, and incubated for 2 min. The reaction mixtures were then diluted to a final volume of 5 mL with ethanol. Absorbance measurements were acquired at 500 nm (λ_{max}) using a UV-vis spectrophotometer, with triplicate determinations for each concentration. A calibration curve was generated by plotting the mean absorbance values against Pb^{2+} concentration, and the linear regression equation was derived to calculate the coefficient of determination (R^2). The limit of detection (LOD) and limit of quantitation (LOQ) were calculated using the equations:[35]

$$LOD = \frac{3.3\sigma}{s} \qquad (1)$$

$$LOQ = \frac{10\sigma}{s} \qquad (2)$$

where σ represents the standard deviation of the intercept from the calibration equation and s is the slope of the calibration curve.

2.5.2 Accuracy and precision evaluation of Pb^{2+} determinations. To assess the accuracy and precision of the **S9b** chemosensor, water samples were collected from three distinct sources in Agbowo Express, Akinyele (Ibadan, Nigeria): well water, river water, and tap water. Particulate matter was removed by filtration into sterile containers. Baseline Pb^{2+} concentrations were quantified prior to spiking. A lead nitrate stock solution (1000 mg L^{-1}) was prepared by dissolving 10 mg of lead nitrate in 10 mL of each filtered water sample. Recovery studies were conducted by spiking the samples with Pb^{2+} at concentrations of 4.68, 7.02, and 8.58 mg L^{-1}. Analyses were performed in quadruplicate using both the **S9b** chemosensor and atomic absorption spectroscopy (AAS).

Accuracy was assessed as percentage recovery, while precision was evaluated *via* relative standard deviation (RSD). Statistical comparisons between the **S9b** and AAS methods were conducted using Student's *t*-test (for means) and the *F*-test (for variances).

2.6 Determination of binding mechanism

A solution of 8.401 mg $Pb(NO_3)_2$ in 2 mL deionized water was added dropwise to 1 mg mL^{-1} *N,N*-dimethylformamide (DMF) solution of **S9b**. The mixture was magnetically stirred for 30 min at ambient temperature. The resulting precipitate was isolated *via* vacuum filtration, washed thoroughly with deionized water, and air-dried. Fourier-transform infrared (FT-IR) spectroscopy was employed to compare the spectra of free **S9b** and its Pb^{2+} complex, enabling identification of functional groups involved in Pb^{2+} coordination.

2.7 Reversibility experiment

To investigate the reversibility of Pb^{2+} binding to **S9b**, 134 µL of **S9b** (2.3428 mM) and 66 µL of Pb^{2+} solution (2.3428 mM) were combined in a vial. The mixture was vortex-mixed for 10 s and

incubated for 2 min at ambient temperature. Subsequently, 134 µL of disodium ethylenediaminetetraacetic acid (Na$_2$EDTA; 2.3428 mM) was introduced, followed by vortex-mixing and incubation for 2 min. The final solution was diluted to 5 mL with ethanol, and its UV-vis absorption spectrum was recorded across 200–700 nm to assess spectral changes induced by competitive EDTA chelation.

2.8 Selectivity assessment of S9b toward Pb^{2+} in the presence of competing metal ions

To evaluate the selectivity of **S9b** for Pb^{2+}, 134 µL of **S9b** stock solution (2.3428 mM) and 5 molar equivalents (eq.) of Pb^{2+} were added to each of 13 vials. The mixtures were vortex-mixed for 10 s, followed by the addition of 5 eq of competing metal ions: Ag^+, Co^{2+}, Cu^{2+}, Fe^{2+}, Fe^{3+}, Na^+, K^+, Ni^{2+}, Hg^{2+}, Ca^{2+}, Zn^{2+}, Mg^{2+}, and Al^{3+}, to individual vials. After vortex-mixing and incubation for 2 min at ambient temperature, each solution was diluted to 5 mL with ethanol. Absorbance measurements were recorded at 500 nm (λ_{max}) using a UV-vis spectrophotometer. Triplicate determinations were performed, and the mean absorbance values (±standard deviation) were plotted on a bar chart to compare the response of **S9b**–Pb^{2+} complexes in the presence of interfering ions.

2.9 Density functional theory

Density functional theory (DFT) calculations were conducted using the Gaussian 09 program, Revision C.01. The gas-phase geometry of **S9b**, initially constructed using GaussView software, was optimized using the Coulomb-attenuating hybrid exchange–correlation functional (CAM-B3LYP) with the 6-311++G (d,p) basis set, assuming a singlet spin state and neutral charge. For the **S9b**–Pb^{2+} complex, geometry optimization was performed using the LanL2DZ effective core potential and basis set (with 5D and 7F angular momentum functions) under a +2 charge state.

3. Results and discussion

3.1 Synthesis of S9b (1-amino-4-[(E)-2-(8-hydroxyquinolin-5-yl)diazen-1-yl]-9,10-dihydroanthracene-9,10-dione)

S9b was synthesized by first diazotizing of 1,4-diaminoanthracene-9,10-dione (I) at one of the aromatic amines with moderate acid concentration of 1 M hydrochloric acid and subsequent diazocoupling of the diazonium product (II) with 8-hydroxyquinoline (III) as shown in Scheme 1. Diazocoupling took place at *para* position to the phenolic group of (III). The chemical structure of **S9b** was confirmed by spectroscopic techniques.

3.2 Characterization of S9b

Violet; yield: 51.55%; FTIR (ATR, ν, cm^{-1}): C=O (1630), N=N (1500), N–H (3400, 3290), C–N (1281), C=N (1580); ^{1}H NMR (600 MHz, acetone): δ 7.74 (dd, J = 5.7, 3.3 Hz, 1H, H-2), 7.69 (d, J = 8.3 Hz, 1H, H-4), 7.63–7.66 (m, 1H, H-3), 7.56 (d, J = 8.6 Hz, 1H, H-3′), 7.46 (d, J = 2.4 Hz, 1H, H-6), 7.28–7.25 (m, 2H, H-5′, 8′), 7.24 (d, J = 2.6 Hz, 1H, H-2′), 7.19 (d, J = 7.1 Hz, 1H, H-7), 7.16
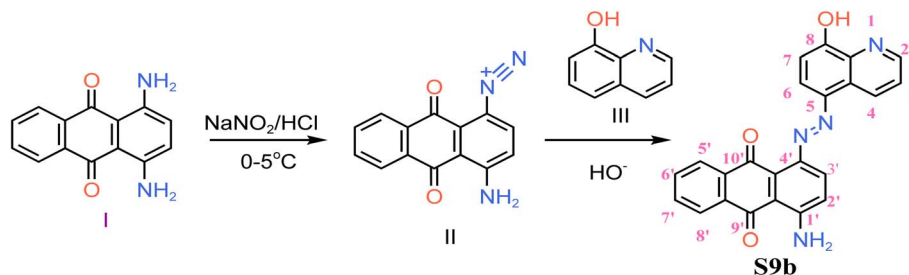
Scheme 1 Synthetic routes of **S9b**.

(dd, J = 7.3, 2.7 Hz, 2H, H-6′, 7′), 3.60 (s, 2H, H-11); ^{13}C NMR (600 MHz, acetone): δ 139.815, 133.433, 131.981, 130.525, 130.280, 129.597, 129.066, 128.993, 128.478, 127.704, 127.433, 126.910, 126.570, 125.401, 124.858, 119.824, 114.604; MS (ESI, m/z): 395.1 [M$^+$ + H]. Anal. calcd. $C_{23}H_{14}O_{13}N_4$: C, 70.04; H, 3.57; O, 12.18; N, 14.20; found: C, 70.10; H, 3.55; O, 12.14; N, 14.26. The spectra are shown in the ESI† (Fig. S1–S5).

3.3 Spectroscopic response of S9b to cations

The interaction of **S9b** with nitrate salts of Ag^+, Co^{2+}, Cu^{2+}, Fe^{2+}, Fe^{3+}, Na^+, K^+, Ni^{2+}, Pb^{2+}, Hg^{2+}, Ca^{2+}, Zn^{2+}, Mg^{2+}, and Al^{3+} in ethanol was investigated using UV-vis absorption spectroscopy. Free **S9b** exhibited a rosy-brown coloration in ethanol, which changed to a distinct sandy-brown exclusively upon addition of

Pb^{2+} (Fig. 1a). No significant color changes were observed with other cations, even at five equivalents.

UV-vis spectral analysis (Fig. 1b) further corroborated this color behavior. While the absorption profiles of **S9b** remained largely unperturbed in the presence of Ag^+, Co^{2+}, Cu^{2+}, Fe^{2+}, Fe^{3+}, Na^+, K^+, Ni^{2+}, Hg^{2+}, Ca^{2+}, Zn^{2+}, Mg^{2+}, and Al^{3+}, Pb^{2+} induced a pronounced red shift accompanied by a hyperchromic effect at 500 nm. This spectral pattern is attributed to ligand-centered electronic transitions ($n \rightarrow \pi^*$) and potential d–d interactions facilitated by the coordination geometry of the **S9b**–Pb^{2+} complex. The wavelength of maximum absorptivity difference (500 nm) was subsequently utilized for quantitative Pb^{2+} determination.

The unique behavior of Pb^{2+} likely arises from its larger ionic radius, higher polarizability, and soft Lewis acid character,
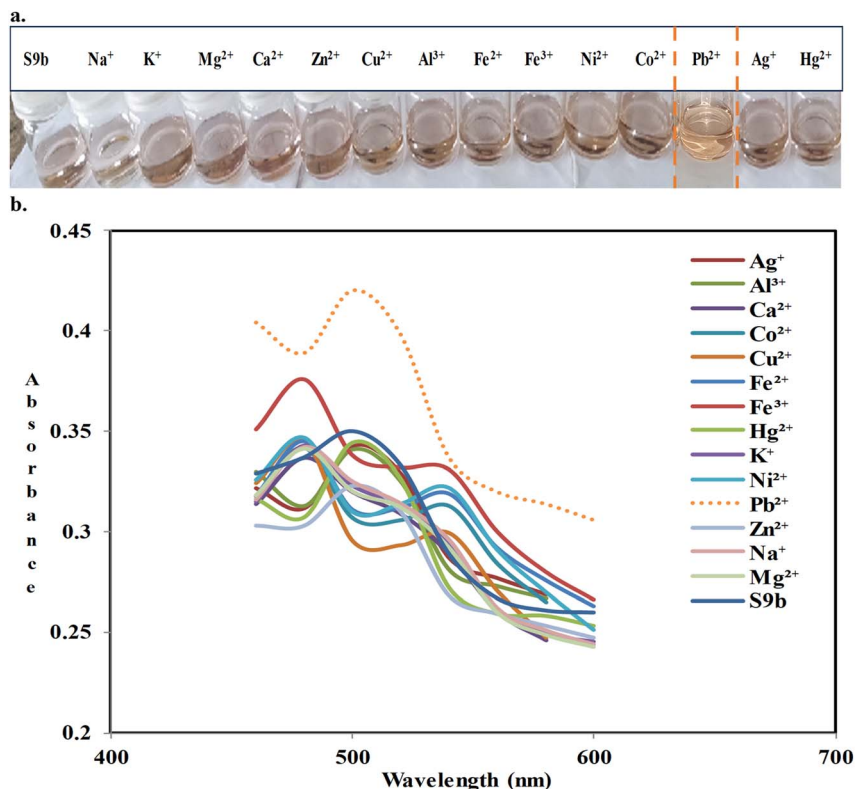

Fig. 1 Color changes of **S9b** in the presence of lead(II) ions and other cations in ethanol, pH 6 (a); overlaid spectra of **S9b** (0.9230 mg mL^{-1}) in the presence of five equivalents of each cation solution in ethanol (b).

which enhance its complementarity with the portal of electron-rich phenolic hydroxyl and quinoline nitrogen moieties of **S9b**. Additionally, the ability of Pb^{2+} to adopt distorted coordination geometries due to the inert pair effect (retention of its $6s^2$ electrons) may stabilize distinct electronic transitions that other cations can't.

3.4 Job's plot experiment

To elucidate the binding stoichiometry between **S9b** and Pb^{2+}, a Job's plot of continuous variations was constructed by recording the absorbance at 500 nm across a series of solutions with varying mole ratios of **S9b** to Pb^{2+} (Fig. 2a). The plot exhibited a distinct maximum at a mole fraction of **S9b** of 0.67, beyond which the absorbance plateaued, indicating saturation of the interaction. This inflection point corresponds to a $2:1$ binding stoichiometry (**S9b** : Pb^{2+}), consistent with the coordination of two ligand molecules (**S9b**) to a single Pb^{2+} ion.

3.5 Response time and selection of diluting solvents

For colorimetric sensors, rapid response kinetics are critical for real-time applications. To evaluate the behavior of **S9b** toward Pb^{2+}, the absorbance of the **S9b**–Pb^{2+} complex was monitored at 500 nm over 30 minutes in ethanol. As shown in Fig. 2b, the absorbance increased sharply within the first 2 minutes, reaching a maximum intensity, followed by a gradual decline. This suggests that the binding equilibrium between **S9b** and Pb^{2+} is established rapidly, with optimal signal stability achieved at 2 minutes. The subsequent decrease in absorbance may arise from slow ligand dissociation under prolonged ambient conditions. Therefore, the reaction between **S9b** and Pb^{2+} was allowed to stay for 2 minutes.

The performance of **S9b** as a Pb^{2+} sensor was also evaluated across solvents of varying polarity and donor properties, including ethanol, methanol, acetone, DMSO, and DMF. Notably, the **S9b**–Pb^{2+} complex exhibited no significant variation in coloration or absorbance intensity at 500 nm across these solvents. Hence, ethanol was selected as the reaction medium due to its low toxicity, biodegradability, and cost-effectiveness, aligning with green chemistry principles.

3.6 Effects of pH on reaction between S9b and lead(II) ions

Azo-based chemosensors are inherently sensitive to pH variations due to the protonation equilibria of their functional groups, which modulate electronic transitions and metal-
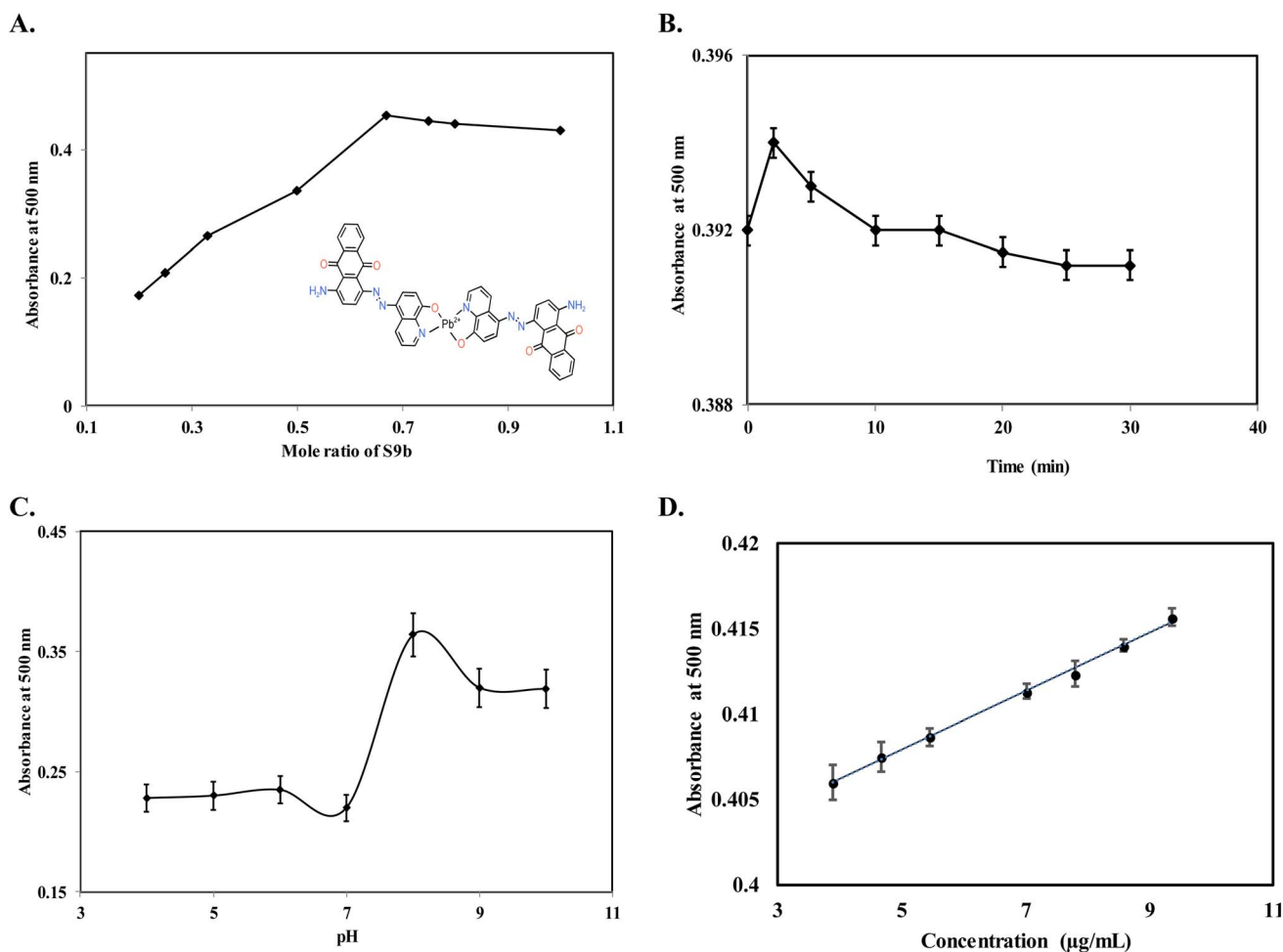

Fig. 2 Job's plot for **S9b** with Pb^{2+}. (Inset) Proposed structure of **S9b**–Pb^{2+} (A); chelating time of reaction of **S9b** and Pb^{2+} (B); reaction pH between **S9b** and Pb^{2+} (C) and linear response of 24.74 μg mL^{-1} **S9b** to varying concentrations of Pb^{2+} (3.90–9.36 μg mL^{-1}) in ethanol (D).

binding affinity.[33] To evaluate the pH response of **S9b** as a Pb^{2+} sensor, the absorbance response was investigated across a pH range of 4–10 (Fig. 2c). The sensor exhibited stable absorbance values between pH 4 and 6, followed by a sharp increase at pH 8, with maximal signal intensity observed under basic conditions.

This pH-dependent behavior is attributed to structural and electronic changes in **S9b**. In alkaline media (pH > 7), deprotonation of the hydroxyl group on the 8-hydroxyquinoline moiety generates a phenoxide ion, enhancing electron delocalization across the conjugated azo-chromophore. The resulting electron-rich phenoxide strengthens coordination to Pb^{2+} *via* lone pair donation, likely forming a stable chelate complex that amplifies ligand-to-metal charge transfer (LMCT) transitions. Conversely, under acidic conditions (pH < 6), protonation of the azo bridge (–N=N–) disrupts conjugation, diminishing the chromophore's π-electron system and reducing its ability to engage in electronic transitions, thereby lowering absorbance.

Notably, while the highest absorbance occurred at pH 8, practical considerations necessitated optimum **pH 6** for Pb^{2+} determination. Basic pH levels risk hydroxide precipitation of Pb^{2+} (as $Pb(OH)_2$), complicating quantification, whereas overly acidic conditions impair sensor performance. The choice of pH 6 balances optimal chromophore activity with minimized interference from lead hydrolysis, ensuring reliable detection in environmentally relevant aqueous systems.

3.7 Analytical performance of S9b for Pb^{2+} detection

The quantitative relationship between the absorption intensity of **S9b** and Pb^{2+} concentration was established *via* a linear regression analysis (Fig. 2d). The sensor exhibited a linear response ($R^2 = 0.9967$) within the Pb^{2+} concentration range of 3.90–9.36 μg mL^{-1}, as described by the equation: $y = 0.0017x + 0.3993$ ($n = 3$). Where y represents absorbance and x is Pb^{2+} concentration (μg mL^{-1}). The high correlation coefficient adheres to the ICH Q2(R1) guideline requirement for linearity ($R^2 \geq 0.98$),[36] validating the method's suitability for quantitative analysis.

The calculated binding constant (k), 3.07×10^4 L^2 g^{-2}, was obtained from modified Benesi–Hildebrand's eqn (3) based on $2:1$ stoichiometry:[37] The plot of $\frac{A_{max} - A_o}{A - A_o}$ against $\frac{1}{[Pb^{2+}]^2}$ is shown in the ESI (Fig S6†).

$$\frac{1}{A - A_o} = \frac{1}{A_{max} - A_o} + \frac{1}{K(A_{max} - A_o)}\left(\frac{1}{[Pb^{2+}]^2}\right) \quad (3)$$

Further modification of eqn (3) gives eqn (4)

$$\frac{A_{max} - A_o}{A - A_o} = 1 + \frac{1}{K}\left(\frac{1}{[Pb^{2+}]^2}\right) \quad (4)$$

$$\text{Then from Fig S6, the binding constant}(k) = \frac{\text{intercept}}{\text{slope}} \quad (5)$$

The constant reflects strong affinity between **S9b** and Pb^{2+}, consistent with reported values for Pb^{2+} sensors.[38,39] Sandell's sensitivity, a measure of method detectability, was calculated as 58.823 ng cm^{-2}, indicating that a low concentration of Pb^{2+} can induce a measurable absorbance change.

The limit of detection (LOD) and limit of quantification (LOQ) were determined using the formulae 3.3 σ/s and $10\sigma/s$, respectively, where σ is the standard deviation of the intercept of the calibration equation and s is the slope of the calibration curve. The LOD and LOQ values of 1.55 μg mL^{-1} and 4.71 μg mL^{-1}, respectively, demonstrate **S9b**'s capability to detect Pb^{2+} at the part-per-million (ppm) level. While this sensitivity aligns with conventional colorimetric sensors, future modifications to the **S9b** structure by introducing electron-withdrawing groups or auxiliary binding sites could enhance detection to sub-ppm levels for trace environmental or biological applications.

3.8 Binding mechanism of S9b with lead(ɪɪ) ions

To probe the binding mechanism between **S9b** and Pb^{2+}, Fourier-transform infrared (FTIR) spectroscopy was conducted.
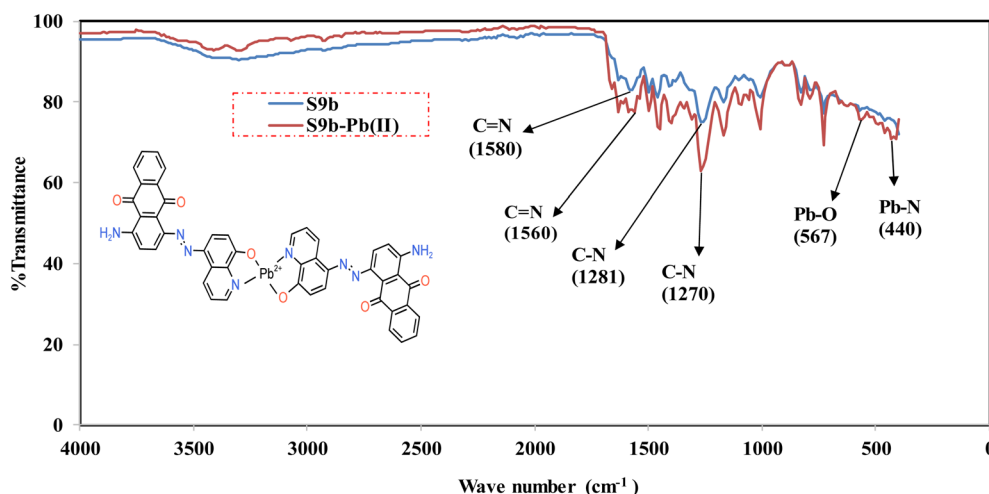

Fig. 3 Overlaid FTIR Spectra of **S9b** and **S9b**−Pb^{2+}.

Comparative analysis of the FTIR spectra of free **S9b** and its Pb^{2+} complex (Fig. 3) revealed distinct shifts in key vibrational modes. The C–N and C=N stretching vibrations of the azo-quinoline moiety, originally observed at 1281 cm^{-1} and 1580 cm^{-1} in free **S9b**, shifted to 1270 cm^{-1} and 1560 cm^{-1}, respectively, in the Pb^{2+} complex. These shifts indicate electron donation from the nitrogen and –OH groups of quinoline to Pb^{2+}, weakening the bond strengths and reducing their vibrational frequencies.

Notably, the O–H bending vibration at 1371 cm^{-1}, associated with the phenolic hydroxyl group of 8-hydroxyquinoline in free **S9b**, diminished significantly in the complex, suggesting deprotonation of the hydroxyl group upon coordination to Pb^{2+}. This is further corroborated by the emergence of new vibrational bands at 567 cm^{-1} and 440 cm^{-1}, assigned to Pb–O and Pb–N stretching modes, respectively. These findings confirm direct coordination of Pb^{2+} to both the deprotonated phenolic oxygen and the quinoline nitrogen of **S9b**.

In contrast, the carbonyl (C=O) stretching vibration of the anthraquinone core remained unaltered in both free **S9b** and its Pb^{2+} complex, indicating no involvement of the ketonic oxygen in metal binding. This observation aligns with prior studies on anthraquinone-based sensors, where the carbonyl group retains its electronic independence during complexation.[39,40] The FTIR data support a binding mechanism wherein Pb^{2+} interacts selectively with the nitrogen and the deprotonated phenolic oxygen of the 8-hydroxyquinoline moiety. This bidentate coordination mode enhances the stability of the **S9b**–Pb^{2+} complex, consistent with the 2:1 stoichiometry inferred from Job's plot analysis (Fig. 2a) and the UV-vis spectral changes.

3.9 Reversibility and reusability of S9b

To assess the reversibility of the **S9b**–Pb^{2+} interaction, the complex was treated with disodium ethylenediaminetetraacetate (Na_2EDTA), a strong chelating agent with high affinity for Pb^{2+}. Upon addition of Na_2EDTA, the hyperchromic absorbance band of the **S9b**–Pb^{2+} complex at 500 nm diminished completely, and the resulting spectrum became superimposable with that of free **S9b** (Fig. 4). This spectral restoration confirms the displacement of Pb^{2+} from the complex by EDTA, regenerating unbound **S9b** through competitive chelation.

The reversibility of the binding interaction underscores the dynamic equilibrium between **S9b** and Pb^{2+}, while the restoration of the ligand's original spectral profile demonstrates its structural integrity post-metal release. These findings suggest that **S9b** can be reused in sensing applications, as the ligand retains its functionality after Pb^{2+} removal. Furthermore, the ability to regenerate **S9b** via EDTA treatment highlights its potential for recyclability in cost-effective or continuous monitoring systems.

3.10 Analytical application of S9b in environmental samples

The azo-based chemosensor **S9b** was successfully validated for the determination of Pb^{2+} in three environmental water samples (well, river, and tap water). Initial analysis confirmed the absence of detectable Pb^{2+} in unspiked samples. To evaluate accuracy and precision, known concentrations of Pb^{2+} were spiked into the samples, and recoveries were calculated using both **S9b** and atomic absorption spectroscopy (AAS) (Table 1).

The **S9b** method demonstrated excellent accuracy, with recovery percentages ranging from 100.03% to 103.11%, and high precision, reflected by relative standard deviation (RSD) values of 0.06% to 2.07%. These results affirm the practicality of **S9b** for Pb^{2+} quantification in aqueous matrices. Statistical validation via F- and t-tests further confirmed the method's reliability: p-values exceeding 0.05 for both tests indicated no
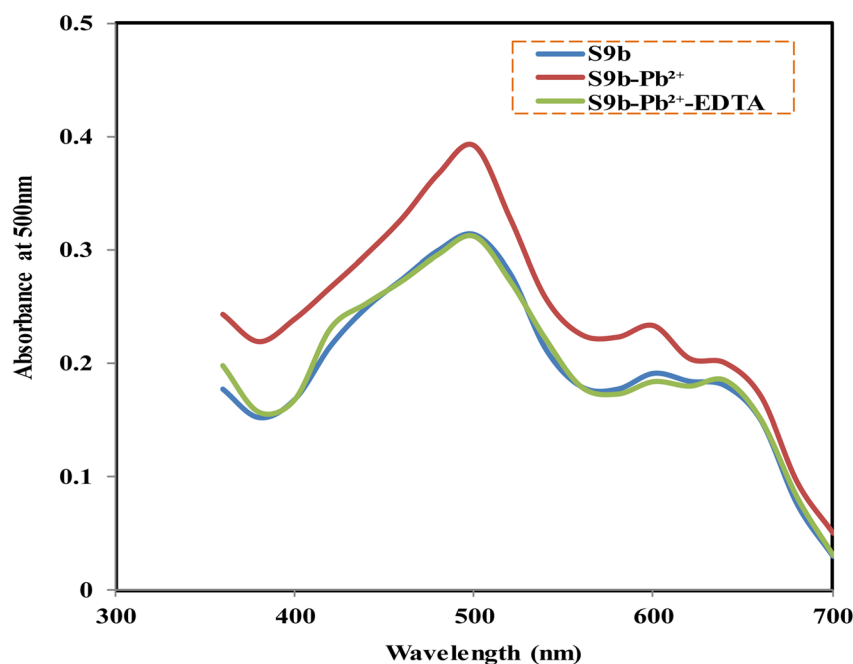

Fig. 4 Overlaid spectra of **S9b**, **S9b**−Pb^{2+}, and **S9b**−Pb^{2+}−EDTA.

Table 1 Accuracy and precisions of lead spiked into different water sources

| Water source | Spiked (mg L^{-1}) | S9b method | | AAS | | t test | F test |
		% Recovery[a]	RSD	% Recovery[a]	RSD		
Well	4.68	103.11	0.50	99.11	0.10		
	7.02	103.28	0.46	101.37	0.15	0.88	0.93
	8.58	100.19	0.64	99.63	0.06		
River	4.68	103.63	0.31	100.35	0.05		
	7.02	102.12	0.12	101.18	0.12	0.99	0.79
	8.58	100.89	1.16	103.84	0.15		
Tap	4.68	102.57	2.07	101.25	1.25		
	7.02	100.74	0.54	102.07	0.98	0.79	0.27
	8.58	100.03	0.06	103.18	0.37		

[a] Quadruplicate determinations.

significant difference between the means and variances of the **S9b** and AAS datasets. Furthermore, this statistical equivalence underscores **S9b** as a viable alternative to AAS for Pb^{2+} detection in environmental monitoring.
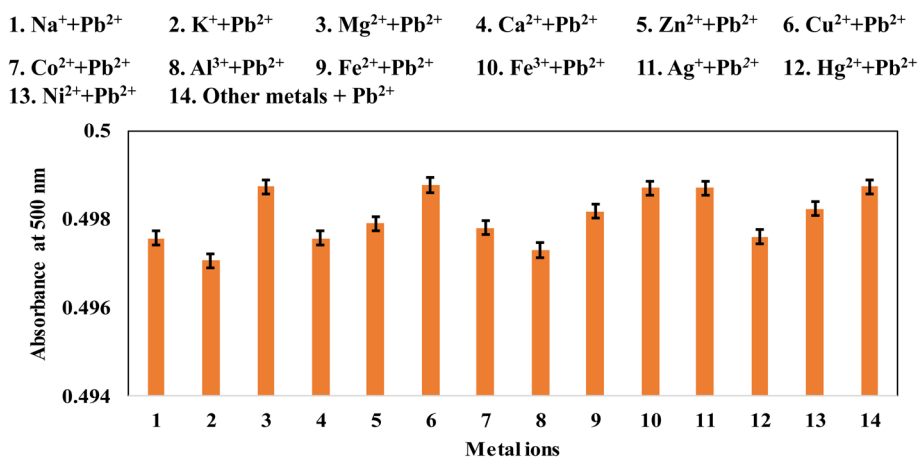
3.11 Competition experiments

To evaluate the selectivity of **S9b** for Pb^{2+} in complex matrices, competition experiments were conducted with potential interfering cations (Ag$^+$, Co^{2+}, Cu^{2+}, Fe^{2+}, Fe^{3+}, Na$^+$, K$^+$, Ni^{2+}, Hg^{2+}, Ca^{2+}, Zn^{2+}, Mg^{2+}, and Al^{3+}). The absorbance intensity of the **S9b**–Pb^{2+} complex at 500 nm was monitored in the presence of these cations at 5 eq concentrations to Pb^{2+} (Fig. 5). Notably, the absorbance signal for Pb^{2+} remained largely unaffected by the coexistence of competing ions, even at elevated concentrations. This insensitivity to interference underscores the selectivity of **S9b** for Pb^{2+}. These findings confirm that **S9b** retains its analytical performance in multicomponent systems, making it suitable for Pb^{2+} detection in environmentally water samples where competing ions are ubiquitous.

3.12 DFT studies

To corroborate the proposed 2 : 1 binding stoichiometry (**S9b** : Pb^{2+}) inferred from Job's plot analysis, density functional theory (DFT) calculations were performed on **S9b** and its Pb^{2+} complex.

The optimized geometries of free **S9b** and the **S9b**–Pb^{2+} complex (Fig. 6a and 7a) revealed significant structural reorganization upon metal coordination. Free **S9b** adopts a twisted conformation, evidenced by a dihedral angle (N39–C25–C30–O37) of 0.2396°, which transitions to a fully planar configuration in the Pb^{2+} complex. This planarization facilitates chelation of Pb^{2+} via the nitrogen of the quinoline heterocycle and the deprotonated phenolic oxygen, forming a stable six-membered coordination ring.

Electronic structure analysis further elucidated the spectral behavior of the complex. The energy gaps (ΔE) for the three lowest-energy transitions (HOMO → LUMO, HOMO+1 → LUMO+1, HOMO+2 → LUMO+2) exhibited an ascending trend (Fig. 6 and 7), with ΔE values for **S9b**–Pb^{2+} consistently lower than those of free **S9b**. This reduction in ΔE aligns with the observed bathochromic shift in UV-vis spectra, as smaller energy gaps correlate with longer absorption wavelengths.[41] Additionally, the enhanced oscillator strength of these transitions explains the hyperchromic effect in the complex, attributed to intensified ligand-to-metal charge transfer (LMCT) upon Pb^{2+} binding. The DFT results rationalize the experimental UV-vis and FTIR data, affirming the proposed 2 : 1 stoichiometry and binding mode (Fig. 2, inset). The planarization of **S9b**, coupled with electronic delocalization in the Pb^{2+} complex, underscores the ligand's electronic complementarity for selective Pb^{2+} sensing.

1. Na$^+$+Pb^{2+} 2. K$^+$+Pb^{2+} 3. Mg^{2+}+Pb^{2+} 4. Ca^{2+}+Pb^{2+} 5. Zn^{2+}+Pb^{2+} 6. Cu^{2+}+Pb^{2+}
7. Co^{2+}+Pb^{2+} 8. Al^{3+}+Pb^{2+} 9. Fe^{2+}+Pb^{2+} 10. Fe^{3+}+Pb^{2+} 11. Ag$^+$+Pb^{2+} 12. Hg^{2+}+Pb^{2+}
13. Ni^{2+}+Pb^{2+} 14. Other metals + Pb^{2+}

Fig. 5 Absorption changes of **S9b** (24.74 μg mL^{-1}) with Pb^{2+} (5 equivalents) and metal ions (5 equivalents) in ethanol.

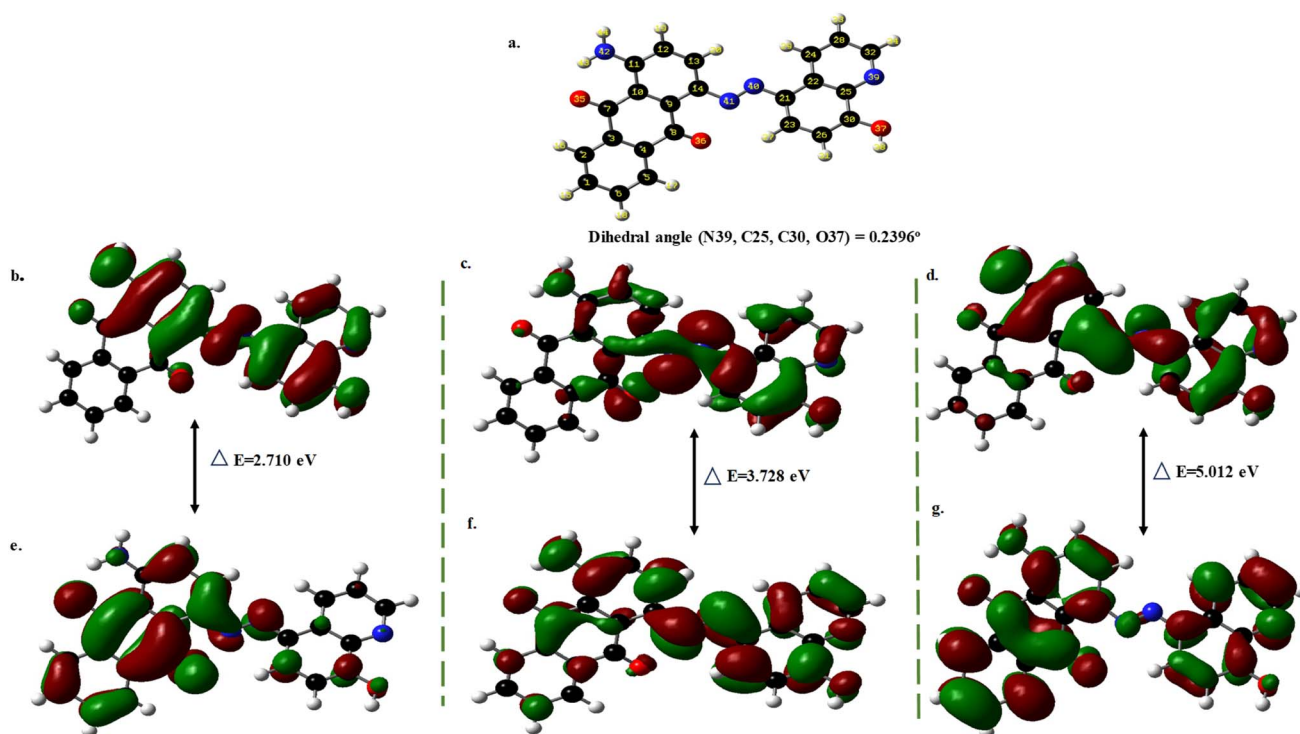Dihedral angle (N39, C25, C30, O37) = 0.2396°

Fig. 6 (a). Optimized geometry of **S9b**; molecular orbitals of energy levels of (b). HOMO (c). HOMO+1 (d). HOMO+2 (e). LUMO (f). LUMO+1 (g). LUMO+2.

3.13 Comparison of S9b method with prior approaches

Table 2 summarizes the response time, limit of detection (LOD), chemosensing millieu, and applications of the anthracene-9,10-

dione azo dye sensor (**S9b**) alongside prior Pb(ɪɪ) detection methods. Similar to existing approaches, the performance of **S9b** was pH-dependent; however, its design integrated practicality and environmental relevance, distinguishing it from
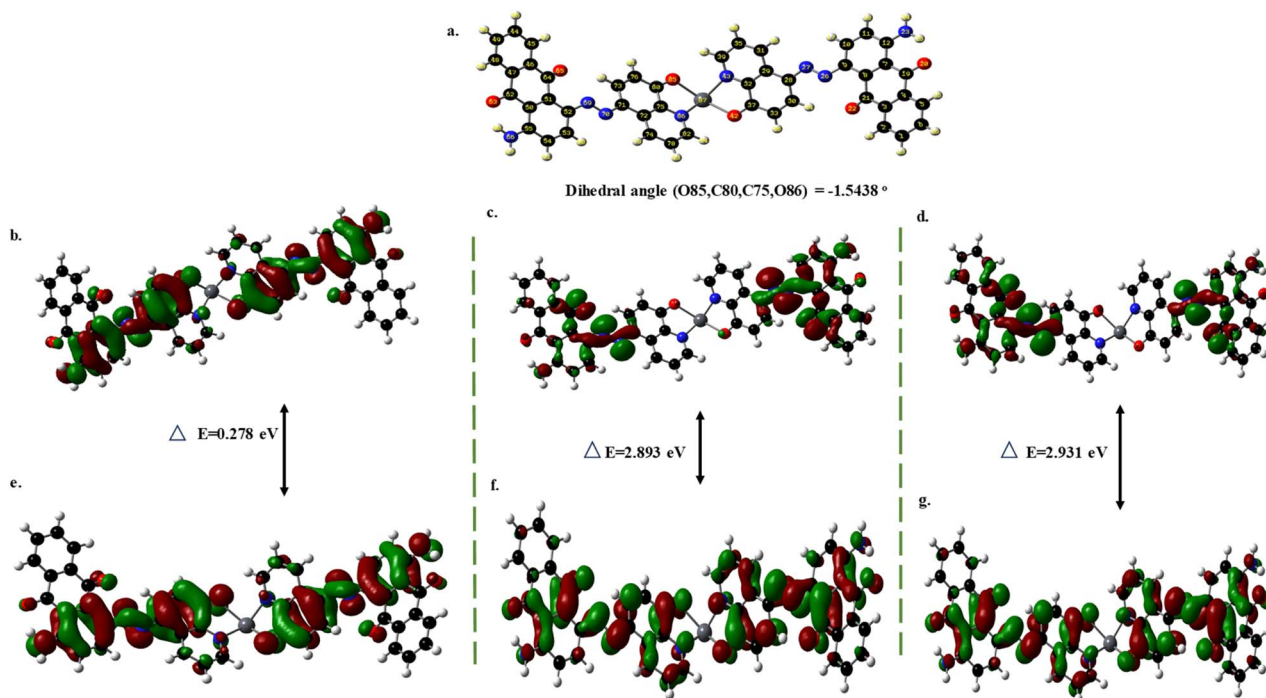

Dihedral angle (O85,C80,C75,O86) = -1.5438 °

Fig. 7 (a). Optimized geometry of **S9b**−Pb^{2+}; molecular orbitals of energy levels of (b). HOMO (c). HOMO+1 (d). HOMO+2 (e). LUMO (f). LUMO+1 (g). LUMO+2.

Table 2 Some colorimetric chemosensors for Pb^{2+} detection

Sensor	Solvent	Reaction time	LOD ($\mu g\ mL^{-1}$)	Analytical range ($\mu g\ mL^{-1}$)	Real samples
Gold nanoparticle[42]	Glycine–NaOH buffer	10 min	9.5	0–10	Lake
Probe-infused polymer monolithic[43]	Solid state	40 s	2.8×10^{-4}	0–0.3	Cigarette samples and water
Azobenzene[26]	Acetonitrile:water (1:1)	30 min	5.44^a	NA	Natural water, live water flea
Functionalized GNP[44]	Aqueous	15 min	5×10^{-4}	0–0.01	Breast milk, drinking water
Schiff base[45]	$MeOH/H_2O$ (3:1)	80 s	6.78×10^{-3}	6×10^{-3} to 41.2^a	Water
Anthracene derived chalcone[39]	$MeOH/H_2O$, 1:1 (v/v)	5 min	0.94^a	NR	Ground and sewage water
Rhodamine 6G[46]	Acetonitrile–water 1:1 (v/v)	<1 min	$2.7 \times 10^{-3\ a}$	$0.01–10^a$	Sea shell foods
Fluophors-gold nanoparticle[47]	Aqueous	40 min	1.1×10^{-4}	0.0016–0.021	Waste and tap water
Curcumin cyclohexanone[37]	Aqueous	5 min	0.5^a	$2–20^a$	Tap and river
Gold nano clusters[48]	Aqueous	1 min	50^a	NR	Deionized water
Anthracene-9,10-dione azo dye (this study)	Ethanol	2 min	$1.55\ (7.49^a)$	3.90–9.36	River, tap and well

^{a} Unit in μM.

conventional systems. The synthesis of **S9b** employed a straightforward diazotization and diazo-coupling protocol, contrasting with the laborious, nanoscience-intensive procedures reported by Saputri et al.,[42] Ratnarathorn et al.,[44] and Wang et al.[47]

The **S9b** sensor exhibited a rapid response time of 2 min for Pb(II) detection in aqueous samples, significantly saving analytical time than the methods of Wang et al. (30 min),[26] Ratnarathorn et al. (15 min),[44] and Wang et al. (40 min).[47] Nevertheless, solid-state composite systems, such as the polymer monolithic probe by Sivaraman et al.[43] and the Rhodamine 6G-based strategy by Wan et al.,[46] achieved sub-minute response times owing to enhanced structural templating that facilitates faster Pb(II) diffusion to binding sites.

Environmental compatibility is a key advantage of **S9b**, as ethanol—a green, water-miscible solvent—serves as the sensing medium. In contrast, methods by Wang et al.,[26] Wan et al.,[46] and Prabhu et al.[39] relied on acetonitrile or methanol, which pose ecological and operational challenges for on-site applications. The LOD of **S9b** ($1.5\ \mu g\ mL^{-1}$) rendered it suitable for monitoring moderately contaminated water systems (ppm-level detection), bridging a critical gap between sensitivity and practicality. While this LOD surpassed those of Saputri et al. ($9.5\ \mu g\ mL^{-1}$)[42] and Bian et al. ($50\ \mu M$),[48] some colorimetric methods exhibited superior sensitivity.[43,44,46]

4. Conclusion

We present **S9b**, a new anthracene-9,10-dione-based azo dye chemosensor for selective and sensitive Pb^{2+} detection in environmental waters. Operating optimally in ethanol (pH 6, 2 min response), **S9b** exhibited a 2:1 binding stoichiometry with Pb^{2+}, validated by Job's plot. The sensor demonstrated selectivity for Pb^{2+} against common interfering cations, reusability via EDTA displacement, and statistical equivalence to AAS in accuracy and precision. FTIR and DFT studies revealed Pb^{2+} coordination through the quinoline nitrogen and deprotonated phenolic oxygen, with spectral shifts rationalized by reduced HOMO–LUMO energy gaps.

While **S9b** shows promise, its detection limit (1.55 ppm) and ethanol dependency limit trace-level analysis in aqueous systems. Future efforts should prioritize structural modifications with electron-withdrawing groups to enhance sub-ppm sensitivity and aqueous compatibility. This study advances anthracene-9,10-dione-based chemosensor design and underscores molecular engineering's role in addressing environmental health challenges through sustainable sensing technologies.

Data availability

The data used to support the findings of the study are available in the article.

Conflicts of interest

There are no conflicts to declare.

Acknowledgements

References

1 M. S. Collin, S. K. Venkatraman, N. Vijayakumar, V. Kanimozhi, S. M. Arbaaz, R. G. S. Stacey, J. Anusha, R. Choudhary, V. Lvov, G. I. Tovar, F. Senatov, S. Koppala and S. Swamiappan, *J. Hazard. Mater. Adv.*, 2022, **7**, 100094.

2 J. E. Gall, R. S. Boyd and N. Rajakaruna, *Environ. Monit. Assess.*, 2015, **187**, 1–21.

3 A. Violante, V. Cozzolino, L. Perelomov, A. G. Caporale and M. Pigna, *J. Soil Sci. Plant Nutr.*, 2010, **10**, 268–292.

4 N. Gupta, D. K. Khan and S. C. Santra, *Bull. Environ. Contam. Toxicol.*, 2008, **80**, 115–118.

5 F. Edition, *WHO Chron.*, 2011, **38**, 104–108.

6 S. J. S. Flora, G. Flora and G. Saxena, in *Lead*, ed. J. S. Casas and J. Sordo, Elsevier Science BV, 2006, vol. 4, pp. 158–228.

7 H. M. Wu, D.-T. Lin-Tan, M.-L. Wang, H.-Y. Huang, C.-L. Lee, H.-S. Wang, Y.-K. Soong and J. L. Lin, *Reprod. Biol. Endocrinol.*, 2012, **10**, 9.

8 D. C. Bellinger, *Birth Defects Res., Part A*, 2005, **73**, 409–420.

9 C. G. Yedjou, C. K. Tchounwou, S. Haile, F. Edwards and P. B. Tchounwou, *Ethn. Dis.*, 2010, **20**, 101.

10 S. L. Zhao, F. S. Chen, J. Zhang, S. B. Ren, H. D. Liang and S. S. Li, *J. Ind. Eng. Chem.*, 2015, **27**, 362–367.

11 G. Billon and C. M. G. Van Den Berg, *Electroanalysis*, 2004, **16**, 1583–1591.

12 M. Sha, Y. Xiaomei and C. Xiumin, *Chem. J. Internet*, 2007, **9**(7), 31.

13 N. C. Munksgaar, G. J. Batterham and D. L. Parry, *Mar. Pollut. Bull.*, 1998, **36**, 527–534.

14 M. R. Cave, O. Butler, J. M. Cook, M. S. Cresser, L. M. Garden and D. L. Miles, *J. Anal. At. Spectrom.*, 2000, **15**, 181–235.

15 M. R. Cave, O. Butler, S. R. N. Chenery, J. M. Cook, M. S. Cresser and D. L. Miles, *J. Anal. At. Spectrom.*, 2001, **16**, 194–235.

16 S. C. Wilschefski and M. R. Baxter, *Clin. Biochem. Rev.*, 2019, **40**, 115–133.

17 S. Sarkar, A. Banerjee, H. Urmi, B. Raju and B. Rajib, *Water Conserv. Sci. Eng.*, 2017, **2**, 121–131.

18 K. M. Lee, X. Chen, W. Fang, J. M. Kim and J. Yoon, *Macromol. Rapid Commun.*, 2011, **32**, 497–500.

19 H. Zheng, X. Q. Zhan, Q. N. Bian and X.-J. Zhang, *Chem. Commun.*, 2013, **49**, 429–447.

20 H. Son, G. Kang and J. H. Jung, *Analyst*, 2012, **137**, 163–169.

21 P. Chen, B. Greenberg, S. Taghavi, C. Romano, D. van der Lelie and C. He, *Angew. Chem., Int. Ed.*, 2005, **44**, 2715–2719.

22 Z. Hu, C. Lin, X. Wang, L. Ding, C. Cui, S. Liu and H. Y. Lu, *Chem. Commun.*, 2010, **46**, 3765–3767.

23 M. Liu, X. Lou, J. Du, M. Guan, J. Wang, X. Ding and J. Zhao, *Analyst*, 2012, **137**, 70–72.

24 Y. Chen and J. Jiang, *Org. Biomol. Chem.*, 2012, **10**, 4782–4787.

25 M. Ghorbanian, S. Asghari and M. Tajbakhsh, *Spectrochim. Acta, Part A*, 2023, **296**, 122652.

26 Y. Wang, S. Hu, Y. Zhang, H. Gong, R. Sun, W. Mao, D. Wang and Y. Chen, *J. Photochem. Photobiol., A*, 2018, **355**, 101–108.

27 A. K. K. Bhasin, P. Chauhan and S. Chaudhary, *Sens. Actuators, B*, 2019, **294**, 116–122.

28 P. Kumar, A. Ghosh and D. A. Jose, *Analyst*, 2019, **144**, 594–601.

29 M. Barzegar, M. F. Mousavi, H. Khajehsharifi, M. Shamsipur and H. Sharghi, *IEEE Sens. J.*, 2005, **5**, 392–397.

30 A. Rahmani, M. Barzegar, M. Shamsipur, H. Sharghi and M. F. Mousavi, *Anal. Lett.*, 2000, **33**, 2611–2629.

31 S. Riahi, M. F. Mousavi, M. Shamsipur and H. A. Sharghi, *Electroanalysis*, 2003, **15**, 1561–1565.

32 X. Li, X. Ma and M. Huang, *Talanta*, 2009, **78**, 498–505.

33 S. O. Olaleye, S. O. Idowu, A. Shakil and M. A. Khan, *RSC Adv.*, 2025, **15**, 3497–3514.

34 J. S. Renny, L. L. Tomasevich, E. H. Tallmadge and D. B. Collum, *Angew. Chem.*, 2013, **52**, 11998–12013.

35 A. Shrivastava and V. B. Gupta, *Chron. Young Sci.*, 2011, **2**, 21–25.

36 European Medicines Agency, ICH guideline Q2(R2) on validation of analytical procedures, https://www.ema.europa.eu/en/documents/scientific-guideline/ich-guideline-q2r2-validation-analytical-procedures-step-2b_en.pdf, accessed 20 May 2025.

37 M. Sadia, J. Khan, R. Khan, S. W. A. Shah, A. Zada, M. Zahoor, R. Ullah and E. A. Ali, *Heliyon*, 2025, **11**, e41125.

38 T. Anand, G. Sivaraman, A. Mahesh and D. Chellappa, *Anal. Chim. Acta*, 2015, **853**, 596–601.

39 J. Prabhu, K. Velmurugan and R. Nandhakumar, *Spectrochim. Acta, Part A*, 2015, **144**, 23–28.

40 S. Kim, S. Gwon and J. Bae, *J. Fiber Soc.*, 2014, **70**, 254–257.

41 L. Hou, X. Kong, Y. Wang, J. Chao, C. Li, C. Dong, Y. Wang and S. Shuang, *J. Mater. Chem. B*, 2017, **5**, 8957–8966.

42 F. A. Saputri, T. S. Aulia, C. Jatmika, R. Iswandana, S. Megantara and V. A. Dhumale, *RSC Adv.*, 2025, **15**, 6931–6937.

43 S. P. Sivaraman, P. Srinivasan, D. K. Madhu, P. Deivasigamani and A. M. Mohan, *J. Hazard. Mater.*, 2025, **487**, 137247.

44 N. Ratnarathorn, O. Chailapakul and W. Dungchai, *Talanta*, 2015, **132**, 613–618.

45 N. Karachi, O. Azadi, R. Razavi, A. Tahvili and Z. Parsaee, *J. Photochem. Photobiol., A*, 2018, **360**, 152–165.

46 J. Wan, K. Zhang, C. Li, Y. Li and S. Niu, *Sens. Actuators, B*, 2017, **246**, 696–702.

47 S. Wang, J. Sun and F. Gao, *Analyst*, 2015, **140**, 4001–4006.

48 R. Bian, X. Wu, F. Chai, L. Li, L. Zhang, T. Wang, C. Wang and Z. Su, *Sens. Actuators, B*, 2017, **241**, 592–600.